

Source-related variations of ground motions in 3-D media: application to the Newport-Inglewood fault, Los Angeles Basin

Haijiang Wang, Heiner Igel, František Gallovič,* Alain Cochard† and Michael Ewald§

Department of Earth and Environmental Sciences, Ludwig-Maximilians-University of Munich, Theresienstraße 41, D-80333 Munich, Germany.

E-mail: igel@geophysik.uni-muenchen.de

Accepted 2008 June 6. Received 2008 June 2; in original form 2007 Jun 11

SUMMARY

Deterministic earthquake scenario simulations are playing an increasingly important role in seismic hazard and risk estimation. Our aim is to calculate a substantial number of different finite-source scenarios, embedded in a 3-D structure for a particular fault or fault system, by pre-calculating numerical Green's functions (NGFs). A large seismic fault is divided into subfaults of appropriate size for which synthetic Green's functions at the surface are calculated and stored. Consequently, ground motions from arbitrary kinematic sources can be simulated for the whole fault or parts of it, by superposition. To illustrate this approach and its functionalities we simulate M 7 (up to 0.5 Hz) scenario earthquakes for a simplified model of the Newport-Inglewood (NI) fault in the Los Angeles (LA) Basin. We quantify the variations of surface ground motion (e.g. peak ground velocity PGV and synthetic seismograms) due to source parameters (e.g. hypocentre location and corresponding slip history). The results show a complex behaviour, with dependence of absolute PGV and its variation on asperity location, source directionality and local structure and demonstrate the necessity to combine 3-D structural and finite-source effects to quantify ground motion characteristics and their variations.

Key words: Earthquake ground motions; Site effects; Computational seismology.

1 INTRODUCTION

The calculation of the complete wavefield for potential large earthquakes in a given seismically active region of known structure will play a central role in reliably estimating shaking hazard (e.g. Olsen & Archuleta 1996; Olsen 2000; Ewald *et al.* 2006). Such calculations will complement hazard estimation, based on probabilistic estimates of seismicity (e.g. Gerstenberger *et al.* 2005) and/or stochastic means, to calculate ground motion scenarios, based on highly simplified physical models (e.g. Beresnev *et al.* 1998; Boore 2003). Earthquake-induced ground motions strongly depend on: (1) the velocity structure, (2) the finite-fault slip histories and (3) source–receiver geometry (directivity effect). The local and regional velocity structure can be estimated and continuously improved using tomographic tools and/or direct measurements (e.g. borehole information). However, the variations due to the rupture processes (stress drop, source mechanisms, rupture velocity, slip velocity, etc.) remains.

This poses a formidable problem when facing the task of estimating ground motions due to ‘scenario earthquakes’ for a specific seismically active region. One has to consider many different slip scenarios for one presumed earthquake to account for rupture related variations. However, the numerical calculation of the complete 3-D wavefield in the observed frequency band for a seismically active basin remains a computationally expensive task. Consequently, ground motion predictions so far were either restricted to simple (e.g. layered) structures allowing the investigation of many finite source scenarios (e.g. Gallovič & Brokešová 2004, 2007a,b; Convertito *et al.* 2006) or complex 3-D media were incorporated, resulting in severe limitations in terms of number of source scenarios that could be investigated (e.g. Olsen & Archuleta 1996; Pitarka & Irikura 1996; Olsen 2000; Ewald *et al.* 2006).

To quantify (finite) source related variations without running the 3-D code for each kinematic source scenario, we propose to generate databases with Green's functions calculated for discrete models of faults or fault systems, for areas with sufficiently well-known 3-D velocity structure and fault locations. The surface ground motions for each subfault excitation are stored, which allows arbitrary finite-fault scenarios to be synthesized at very little computational cost compared with a normal complete 3-D calculation, once the database is available. The opportunity to investigate ground motion variations as a function of many different rupture related parameters for a specific area comes at the price of a sufficiently large number

*Now at: University, Faculty of Mathematics and Physics, Department of Geophysics, V Holesovickach 2, Praha 8, 18000, Czech Republic.

†Now at: Ecole et Observatoire des Sciences de la Terre, 5 rue Rene Descartes, 67084 Strasbourg Cedex, France.

§Now at: PartnerRe, Bellerivestrasse 36, 8034 Zurich, Switzerland.

of initial 3-D simulations for the pre-designed discretized fault and is economical only if the number of synthesized scenarios exceeds the number of numerical Green's function (NGF) calculations. Nevertheless, current and future high-performance computing facilities and massive data storage technology will, no doubt, allow us to develop NGF databases with frequency ranges (e.g. >2 Hz) relevant and of interest to seismologists and earthquake engineers.

In this paper, we present the concept of the NGF method in connection with 3-D numerical tools, discuss the accuracy of the method as a function of subfault size and other earthquake related parameters and present a first application to a model of the Newport-Inglewood (NI) fault in the Los Angeles (LA) basin. We investigate how the ground motion varies with the hypocentre location although final slip is unchanged. The method for calculating the quasi-dynamic rupture process published in Guatteri *et al.* (2004) is adopted to generate slip histories, based on pre-generated sets of random final slip distributions. Finally, we discuss the potential functionalities of this approach for the quantification of local or regional shaking hazard estimates, given the steady increase in available computational resources.

2 NUMERICAL GREEN'S FUNCTIONS: THEORY AND VERIFICATION

In the following, we describe the basic concept of the NGF approach and verify it against high-resolution ('continuous') finite-fault solutions. A target fault plane is divided into equally sized, rectangular subfaults, and for each of these subfaults, the corresponding Green's function is calculated using a double-couple source mechanism (here we restrict ourselves to pure strike-slip excitation). In this way, we compute the response of a medium to double-couple impulse sources distributed along the fault. These responses, called 'NGFs', are then considered as elementary wavefield contributions (or elementary seismograms) to the final synthetic seismogram for the whole earthquake. Note that we use the term Green's function even though in a strict mathematical sense, its use is improper (see eq. 4 below). We use it in connection with our source time function (a Delta function in moment rate) and also to emphasize the relation to the concept of empirical Green's functions developed by Hutchings & Wu (1990) or Bour & Cara (1997). In these approaches, the authors deconvolve the finite-source effects from recordings of small earthquakes, obtaining empirical unite responses (Green's functions) of the medium. Note that other methods, also named 'empirical Green's functions methods', developed by Irikura (1986), Joyner & Boore (1986) or Frankel (1995), do not deconvolve the source effects, which results in a different modelling philosophy that is not used in this study.

The forward calculations can be carried out, using any numerical solution to the 3-D wave propagation problem. Here, we employ a high-order (fourth order in space, second order in time) staggered-grid finite-difference approach (e.g. Igel *et al.* 1995; Graves 1996; Ewald *et al.* 2006), with efficient absorbing boundaries based on the concept of perfectly matched layers (e.g. Collino & Tsogka 2001; Marcinkovich & Olsen 2003) and averaging of elastic moduli and densities to avoid diffraction effects (Moczo *et al.* 2002).

2.1 Theory and verification

Following Aki & Richards (2002), the Green's function, $G_{ip}(x, t, \xi)$, is defined as the i th component of the ground displacement response at position x and time t , excited by a unit impulse force

in p -direction at time $t = 0$, and located at ξ . By taking a time derivative and following the notation of Aki & Richards (2002), the velocity wave introduced by a pure shear fault, Σ , embedded in an isotropic medium, is described by the representation theorem as

$$v_i(x, t) = \iint_{\Sigma} s[\xi, t - \tau(\xi)] \mu(\xi) \tilde{M}_{pq}(\xi) * \frac{\partial G_{ip}(x, t, \xi)}{\partial \xi_q} d\Sigma, \quad (1)$$

where $v_i(x, t)$ is the i th component of velocity at position x and time t . The scalar function $s(\xi, t)$ is the slip rate located at ξ on the fault plane, starting at time $t = 0$ s, and time delay $\tau(\xi)$ describes the arrival of a rupture front propagating from the hypocentre to point ξ . The parameter $\mu(\xi)$ is the shear modulus of the medium. $\tilde{M}_{pq}(\xi) = u_p(\xi)n_q(\xi) + u_q(\xi)n_p(\xi)$, where $u(\xi)$ is the unit normal to the fault and $n(\xi)$ indicates the slip direction. Finally, '*' denotes the time convolution.

The fault plane, Σ , can be divided into N elements, σ_n ($n = 1, \dots, N$), and eq. (1) is then reformulated as

$$v_i(x, t) = \sum_{n=1}^N \iint_{\sigma_n} s(\xi, t) \mu(\xi) \tilde{M}_{pq}(\xi) * \frac{\partial G_{ip}(x, t - \tau(\xi), \xi)}{\partial \xi_q} d\sigma. \quad (2)$$

Note that $\tau(\xi)$ is moved to the argument of the Green's function G_{ip} .

We assume that σ_n is small enough, so that the variations of the individual $s(\xi, t)$, $\mu(\xi)$, $\tilde{M}_{pq}(\xi)$ and $\tau(\xi)$ within σ_n can be neglected. After naming the approximate variables as $s^n(t)$, μ^n , \tilde{M}_{pq}^n and τ^n , eq. (2) is thus approximated as

$$v_i(x, t) \cong \sum_{n=1}^N \left[\tilde{M}_{pq}^n \cdot \iint_{\sigma_n} \frac{\partial G_{ip}(x, t - \tau^n, \xi)}{\partial \xi_q} d\sigma \right] * s^n(t) \mu^n. \quad (3)$$

Similarly, we further neglect the spatial difference between the individual Green's function derivatives, $G_{ip,q}$ (comma stands for the space derivative) within the rupture element and name the representative approximation as $G_{ip,q}^n(x, t - \tau^n)$. Note that the above-mentioned approximations introduce frequency-dependent errors, depending also on receiver position with respect to the source position (directivity, see e.g. Spudich & Archuleta 1987). Finally, we obtain:

$$v_i(x, t) \cong \sum_{n=1}^N [\tilde{M}_{pq}^n \cdot G_{ip,q}^n(x, t - \tau^n)] * s^n(t) \cdot \mu^n \cdot A^n, \quad (4)$$

where A^n is the area of the n th subfault σ_n . We call the part enclosed in the brackets 'NGF' and denote it as $g_i^n(x, t - \tau^n)$. It can be calculated using a slip rate impulse with a given rupture mechanism. Finally, we obtain the basic equation for synthesis of ground motions:

$$v_i(x, t) = \sum_{n=1}^N g_i^n(x, t - \tau^n) * s_i^n(t) \mu^n A^n. \quad (5)$$

Note that the complete $G_{ip,q}$ tensor (see eq. 4) could be stored, to be able to model ground motions, considering various rupture geometries or non-planar faults (Käser & Gallovič 2008). However, it would require three times more in-advance calculations, which we can avoid in our application since we consider a simple (constant) rupture mechanism of pure strike-slip type.

Considering that the goal of this approach is to be able to synthesize—within some limits (e.g. reliable frequency range)—complete ground motions from arbitrary finite-source scenarios on a discretized fault and that the generation of a NGF database is computationally expensive, one should attempt to find a minimum

Table 1. Setup for the homogeneous case.

| | |
|---|----------------|
| Spatial discretization (km) | 1 |
| Time step (s) | 0.0822 |
| <i>S</i> -wave velocity (km s ⁻¹) | 3.9 |
| <i>P</i> -wave velocity (km s ⁻¹) | 6.8 |
| Density (kg m ⁻³) | 2811.0 |
| Time window (s) | 50 |
| Study region (km ³) | 120 × 130 × 45 |
| PML Nodes | 15 |
| Slip velocity (km s ⁻¹) | 2.9 |

number of subfaults necessary to determine the ground motion with sufficient accuracy for a specific earthquake magnitude. As mentioned above, numerical errors in the strong-motion synthesis are introduced when using point sources to represent finite subfaults. To make the NGF method computationally efficient, an optimal (largest) size of the subfault should be first determined. The ‘optimal’ (largest) size of such subfaults is expected to depend on (1) the properties of the ruptures themselves (rupture speed, slip velocity, rise time, etc.), (2) the position of the receiver relative to the rupture propagation (directivity in both strike and dip directions) and (3) the desired frequency band for the synthesized ground motions (related

to the shortest wavelengths in the considered velocity model). This dependence is thoroughly investigated for a homogeneous medium (with parameters shown in Table 1).

At first, seismic motions from a set of double-couple point sources at different depths (1 km vertical separation) are calculated and stored (Fig. 1 top panel, solid circles). The seismograms synthesized at the surface can be used as NGFs. Making use of the translational invariance, NGFs corresponding to a planar vertical fault (Fig. 1 top panel, circles) can be acquired for a given station and finally synthesized to calculate the ground motions for a large earthquake. The parameters for one kinematic rupture test case are defined as follows. The fault dimension of an M_W 7 earthquake is chosen as 36×24 km (which can be evenly subdivided into subfaults of size 2×2 , 3×3 and 4×4 km) and posed such that the strike direction is parallel to the x -axis of the study area. The top of the fault plane is set to be 1 km from the free surface (Fig. 1 top panel) and the two different hypocentres, G1 and G2, are located at the bottom and top left-hand part (red asterisk in Fig. 1 bottom panel), respectively.

The rupture propagates radially from the hypocentre to the other parts of the fault plane, with a constant velocity (Table 1). The scalar moment M_0 in dyn cm is related to the moment magnitude M_W as $\log M_0 = 1.5M_W + 16.05$ (Kanamori 1977). The final

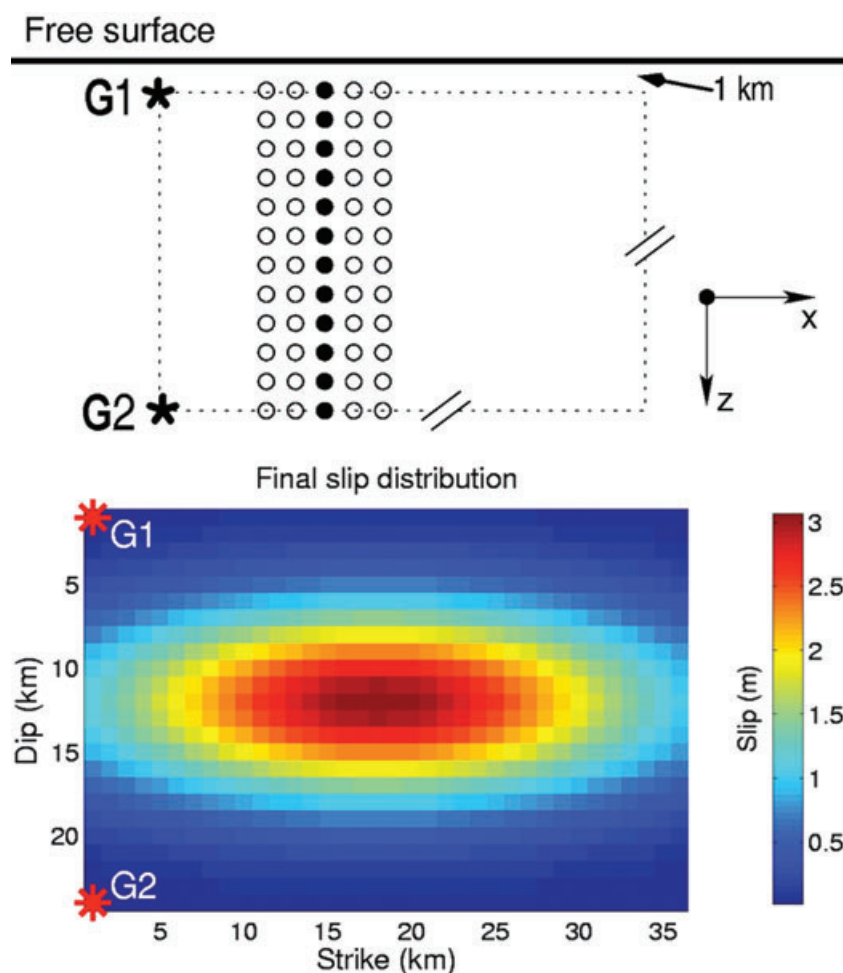


Figure 1. Top panel: Schematic setup for the homogeneous case. The thick black line is the free surface. Black solid circles are the hypocentres of a set of double-couple point sources and the asterisks mark the hypocentres. Bottom panel: Final slip distribution calculated for an M_W 7 earthquake (see Mai & Beroza 2002) with two hypocentres, G1 and G2.

Table 2. Setup for the heterogeneous model in the Los Angeles basin.

| | |
|--|-----------------|
| Spatial discretization (km) | 0.3 |
| Time step (s) | 0.018 |
| Lowest <i>S</i> -wave velocity (km s ⁻¹) | 1.4 |
| Simulation time (s) | 65 |
| Number of cells | 320 × 350 × 100 |
| PML Nodes | 15 |
| Memory (GB) | 5.14 |
| Fault area (km ²) | 18 × 36 |
| Minimum fault depth (km) | 1.5 |

average slip D is calculated as $D = M_0/(\mu A)$. A Gaussian static slip distribution is adopted with the widths in the strike and the dip direction chosen to be 17.2 and 5.8 km, respectively, following the results published in Mai & Beroza (2002, Table 2). The slip-rate function for each subfault in the time domain is assumed to be a boxcar function. Its duration (rise time) is the ratio between the local static slip and the given constant slip velocity (Table 1). The choice to keep constant slip velocity and not, for example, the rise time is somewhat arbitrary. This model is not intended to represent a realistic source, as it serves only as a demonstration of the effects of fault discretization.

The solution with subfault size of 1×1 km is first calculated in the range 0–0.5 Hz and is used as the ‘continuous’ solution. Fig. 2(a) (top left-hand corner) shows two velocity seismograms from different solutions as an example. The misfit energy (ME)

between the seismograms from the differently discretized solutions, that is, subfaults with side-length of 2.0, 3.0 and 4.0 km, respectively, and the ‘continuous’ solution, is used to estimate the accuracy of the discretized solutions.

$$ME = \frac{\sum_{i=1}^{nt} [v_c(i\Delta t) - v_d(i\Delta t)]^2}{\sum_{i=1}^{nt} [v_c(i\Delta t)]^2} \times 100, \quad (6)$$

where $v_c(i\Delta t)$ is the velocity seismogram of the ‘continuous’ solution and $v_d(i\Delta t)$ is that of the discretized solution at time $i\Delta t$, respectively; Δt is the time step.

In Fig. 2(a), the ME distribution on the surface between the solution with 4×4 km subfaults and the ‘continuous’ solution shows the effects of directivity. The y -component is used for this verification because it has larger ME than the other two components in most of the working area (Wang 2007). The largest ME values are found in the triangular area opposite to the direction of rupture propagation and directly above the fault.

Two hypocentres, different in depth (G1 and G2 in Fig. 1), are considered and synthesized with different subfaults sizes. The largest MEs between the solutions of 2×2 , 3×3 and 4×4 km and the ‘continuous’ solution of the entire study area shown in Fig. 2(b), as a function of hypocentre depth. When the hypocentre is deeper, the MEs are smaller. The resulting seismic motions are low-pass filtered (Gaussian filter) with different cut-off periods to

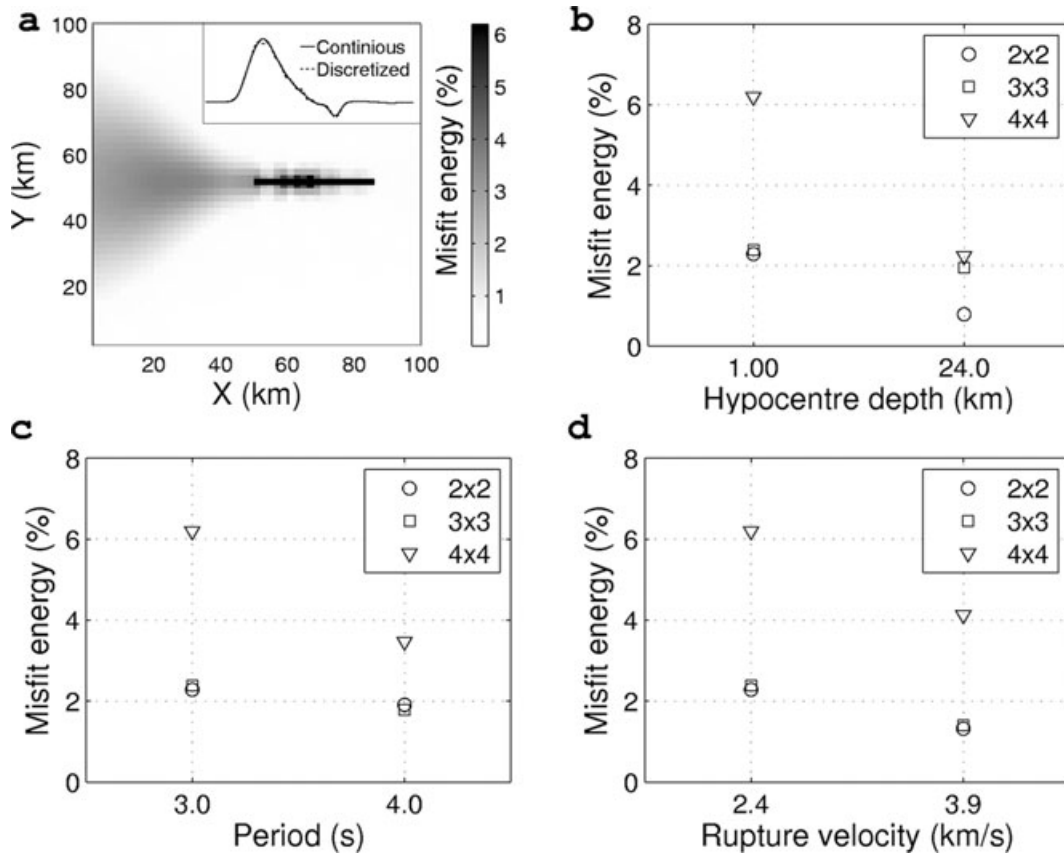


Figure 2. Accuracy of seismogram synthesis as a function of subfault size, hypocentre depth, frequency range and rupture velocity. (a) Map of misfit energy (ME, per cent; see definition in eq. 6) between subfault size 4.0×4.0 km and ‘continuous’ solution (1.0×1.0 km). The rupture propagates along the vertical fault from left- to right-hand side. In the inset, two velocity seismograms are shown. Thick black line (36 km in length) marks the M_W 7 earthquake fault trace. (b) Peak ME as a function of hypocentre depth. (c) Peak ME as a function of cut-off period (Gaussian low-pass filtering). (d) Peak ME as a function of rupture velocity.

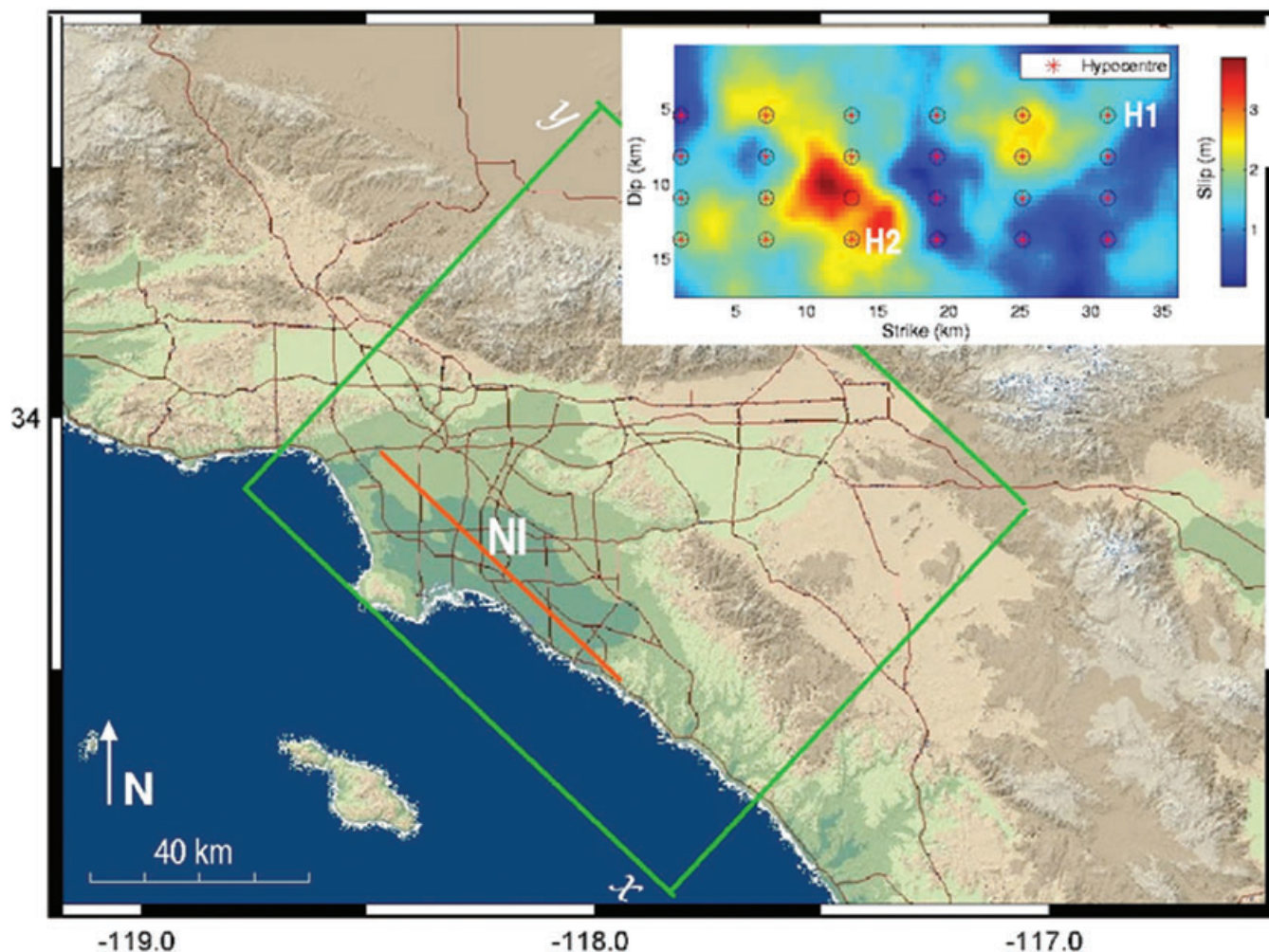


Figure 3. Los Angeles area with modelled region (green rectangle) and the idealized Newport-Inglewood fault (NI, red line). Inset: Final slip distribution of an M_W 7 earthquake on the vertical NI fault plane and hypocentre grid (red asterisks, for investigation of hypocentral effect on ground motion). H1 and H2 represent two hypocentres investigated in detail.

investigate the frequency dependence of ME. The largest ME values (over the whole study area) are shown in Fig. 2(c) as a function of the cut-off period. The MEs increase as higher frequencies are admitted to the solutions. Finally, six M_W 7 earthquakes (two different rupture velocities and three different subfault sizes) are simulated and the resulting largest ME values of the study area are shown in Fig. 2(d), as a function of rupture velocity. From this, we conclude that the accuracy increases with the rupture velocity, keeping all other parameters fixed.

3 STUDY AREA AND NGF DATABASE

We apply the NGF method to the NI fault system, located in the LA basin (Fig. 3). An area of 96×87 km² horizontally, with depth extent 25.5 km vertically, is selected as study area and rotated to have one horizontal grid axis parallel to the NI fault. The velocity model is a simplified version of the elastic part of the SCEC 3-D velocity model for the LA basin (Version 3, Kohler *et al.* 2003). To reduce the computational effort and the size of the database, we truncate the seismic velocities at 1.4 km s⁻¹, which gives a maximum frequency resolution of 0.56 Hz at a grid spacing of 0.3 km (Levander 1988). For illustration, the depth of a shear wave velocity isosurface,

2.0 km s⁻¹, is shown in Fig. 4. The NI fault is chosen for several reasons: it hosted the M 6.4 1933 Long Beach earthquake (Hauksson & Gross 1991), causing serious damage; it is still considered the most probable source for a damaging earthquake to the LA area; the near-vertical plane can be approximated by a vertical plane, to first order, in the numerical calculation and the predominant right-lateral slip can be approximated with a pure strike-slip mechanism (Grant & Shearer 2004). The aim is to test to what extent the NGF concept is useful, and whether it is important to consider both the 3-D structure and scenario earthquakes together in a realistic setting.

The accuracy of the synthesized ground motions as a function of subfault size is investigated for an M_W 7 earthquake, with the computational setup and source parameters given in Table 2. The fault length L and width W are chosen to be 36 and 18 km, respectively. The method published in Guatteri *et al.* (2004) is adopted to produce rupture scenarios for an M_W 7 earthquake. This method is capable of accounting for the accelerating tendency of the crack front due to dynamic loading and the high stress-drop promotion of fast rupture propagation. The quasi-dynamic rupture process calculation starts with a 2-D Gaussian random function (isotropic correlation-length of 5 km). The shear modulus on the fault is kept constant and corresponds to a shear velocity of 3.2 km. The final slip

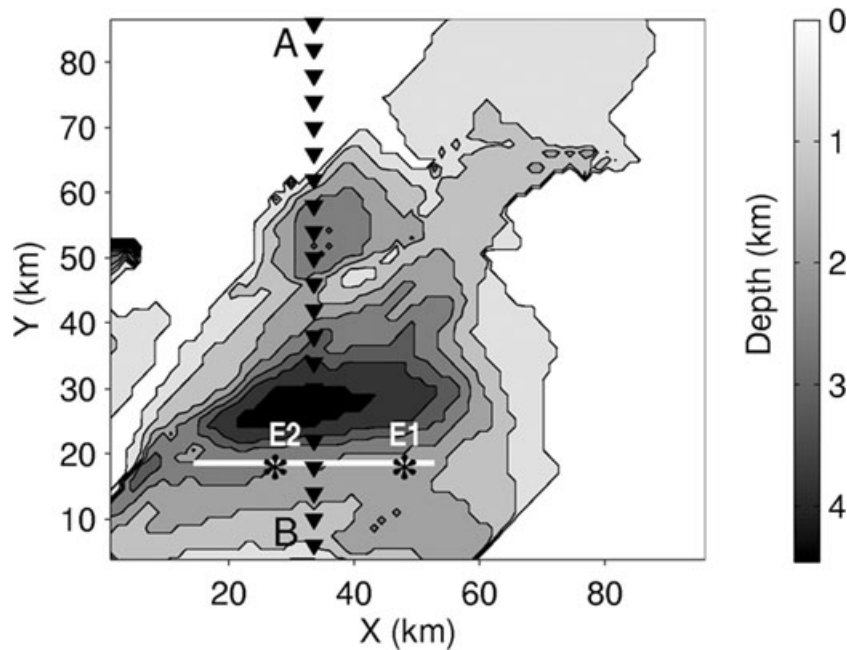


Figure 4. Depth of shear wave velocity isosurface at 2.0 km s^{-1} (grey scale). The thick white line marks the fault trace of the M_W 7 earthquake. Profile AB (black solid triangle) is used for detailed discussion. E1 and E2 are the epicentres corresponding to hypocentres H1 and H2 (Fig. 3 inset).

distribution is shown in Fig. 3 (top right-hand corner). The resulting finite source scenario is simulated with three different equilateral subfaults of side-length 0.3 (120×60 gridpoints, treated as the ‘continuous’ solution, corresponding to the finest grid distance), 1.5 (5×5 gridpoints) and 1.8 km (6×6 gridpoints). The ground motions for the latter two subfault sizes are compared with those for the ‘continuous’ solution.

As an indicator of the accuracy, we compare the peak ground velocity (PGV) over the whole study area, covering frequencies up to 0.5 Hz. The choice of PGV is somewhat arbitrary since other wave-field characteristics could be used (e.g. shaking duration, spectral ordinates, etc.). Fig. 5(a) shows the relative PGV difference, that is, ratio of the PGV difference (x -component) between one discretized solution (sub-fault size of 1.8 km) and the ‘continuous’ solution divided by PGV of the ‘continuous’ solution. Large values are found to happen inside the basin. The largest relative PGV difference is 9.9 per cent in the position of PGV 0.838 m s^{-1} (with an absolute PGV difference of 0.083 m s^{-1}). The waveforms from different solutions are almost identical in the profile shown in Fig. 5(c), with lowest peak correlation coefficient value of 0.988. This can also be seen from the waveform comparison (Fig. 5b) for one single station, where the biggest PGV difference is observed (point P1, Fig. 5a). The maximum amplitude difference between the solution for 1.5 km subfault side-length and the ‘continuous’ one is 0.039 m s^{-1} (4.6 per cent). We consider that this level of accuracy is enough for our case. To be on the safe side, we chose a subfault size of 1.5 km for the generation of the NGF database.

The conclusion about the trend of the accuracy, as a function of cut-off frequency (as shown for the homogeneous case), still holds in the 3-D heterogeneous case. These results justify the choice of the final parameter setup, used to calculate a complete set of NGFs for M_W 7 earthquakes on the NI fault, estimated to cover an area of $69 \times 20 \text{ km}^2$ (Jennings 1994). We calculate a fault area of 40 (along-strike) \times 13 (along-depth) ($60 \times 19.5 \text{ km}^2$ from the northwest edge of the NI fault) subfault NGFs (side length 1.5 km) for a grid spacing of 300 m and seismograms up to 0.5 Hz. This fault area is capable of

covering the historical M 6.4 Long Beach earthquake. The complete NGF database includes the seismograms for the 140×166 equally spaced surface grid at 600 m distance, for the three ground-motion components.

4 SOURCE-RELATED INTEREVENT VARIATIONS OF 3-D GROUND MOTIONS: EFFECT OF HYPOCENTRE LOCATION

The NGF database calculated allows us—within the limits of the method (e.g. frequency range <0.5 Hz) in which the FD method and fault approximation do not bias the results—to synthesize ground motions, from arbitrary strike-slip histories, on the NI fault for the complete study area. A question of considerable practical relevance to estimates of seismic hazard is how variations of the hypocentre location for a given final slip distribution influence the shaking for a ‘scenario’ earthquake of a given magnitude. Among many other possibilities, this is the question we will focus on, in this sample study: we assume the existence of a ‘scenario’ M_W 7 earthquake on the NI fault section from the northwest fault edge and synthesize ground motions for a 4×6 regular grid of hypocentre locations in the seismogenic zone (5–15 km depth), as indicated in Fig. 3 (inset). The same process as in the former section is adopted to produce the needed quasi-dynamic rupture processes with varying hypocentre this time. In this way, the slip velocity functions vary according to chosen hypocentre location. To illustrate the combination of finite-source and basin effects, snapshots of the y -component velocity on the surface are shown in Fig. 6. Most of the energy is radiated in one direction due to the unilateral rupture propagation. Wave propagation is slowed down by the basin (e.g. area A at $T = 28$ s). Basin amplification is observed in area B ($T = 38$ s) and C ($T = 43$ s), where the large ground velocities coincide with the edge of the basin.

In Fig. 7, we show velocity seismograms excited by two hypocentres H1 and H2 (see Fig. 3) on the profile AB (Fig. 4), for different

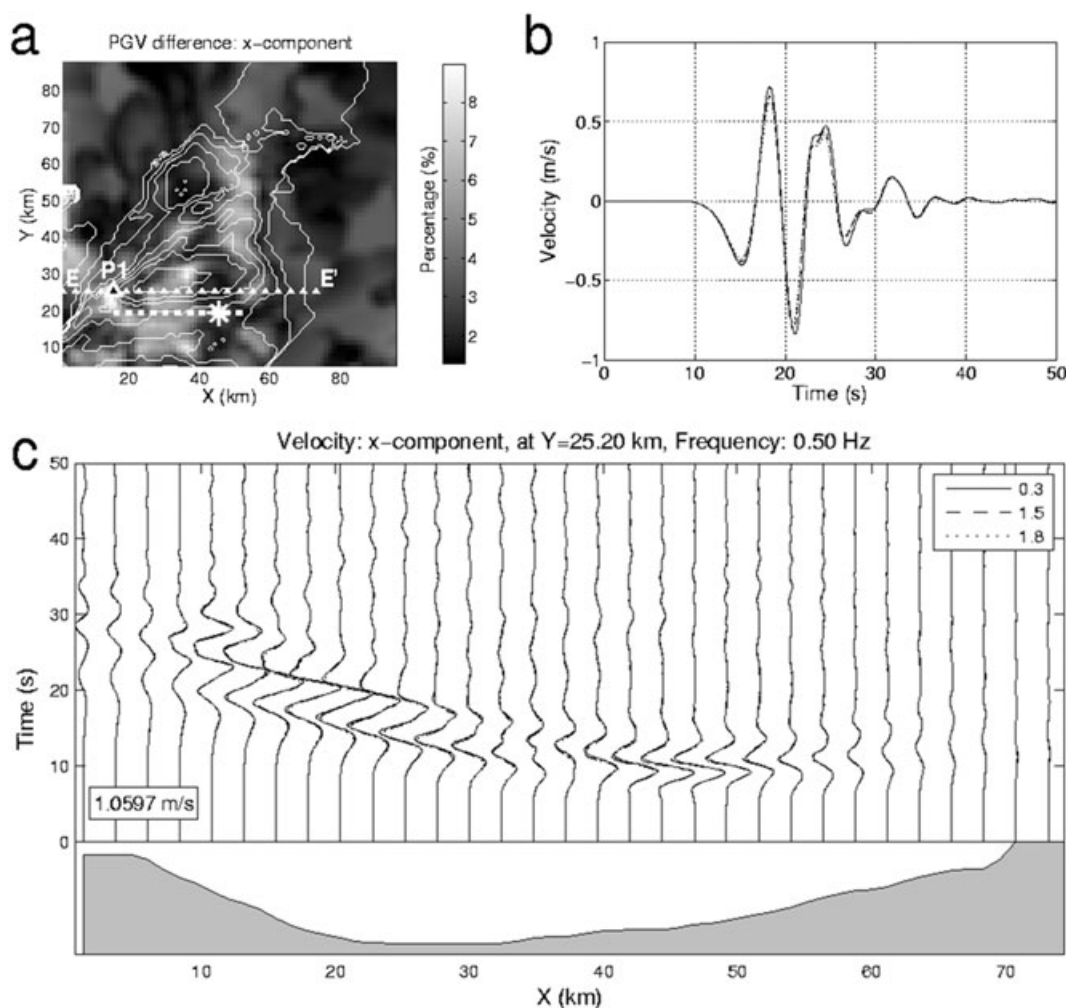


Figure 5. Optimal subfault size determination for an M_W 7 earthquake in LA basin. (a) Relative PGV difference distribution (see definition in text) between the discretized solution of 1.8 km and the ‘continuous’ solution, where dashed thick white line marks the fault trace and the big asterisk, the epicentre. The biggest relative PGV difference is observed at station P1. (b) Velocity seismograms of differently discretized solutions, that is, 0.3, 1.5 and 1.8 km, respectively, for station P1 in (a). (c) Velocity profile, EE’ (a), of differently discretized solutions. The maximum velocity amplitude on this profile is shown with the inset number. The grey area at the bottom illustrates the isosurface depth of shear wave velocity at 2 km s^{-1} .

ground motion components. The corresponding epicentres are marked as E1 and E2 and shown in Fig. 4. The profile crosses the fault trace at $y = 19.0 \text{ km}$ and the sedimentary basin of the study area indicated at the bottom of Fig. 7. In region C, hypocentre H1 (20 km from the profile) results in considerably larger velocities for the y -component (perpendicular to the fault) than does H2 (5 km of fault distance from the profile). In the same region C, H2 leads to much larger velocities than H1 for the x -component of motion. This is likely to be caused by the asperity located between H2 and the profile. Finally, in region D (Fig. 7), H2 leads to larger velocities for both the horizontal components. These results indicate the complex interaction between the position of receivers with respect to hypocentre location, the fault trace and the basin structure and also the sensitivity to specific aspects of the slip history (e.g. asperities).

This simple example illustrates the problems of reliable quantification of expected ground motions for scenario earthquakes without knowledge of structural details, hypocentre location and finite source characteristics. To further highlight this issue, we compare the attenuation of ground motion amplitudes with distance from the fault, obtained by our numerical study, with commonly used empirical relations.

We compare our results to attenuation relationships between the acceleration response spectrum (PSA) and the fault distance developed and widely used for the southern California region (Campbell & Bozorgnia 2003). We compare PSA at a period of 4.0 s, considering that the seismograms are low-pass filtered at period of 2.0 s, which is imposed by the threshold frequency of the finite difference method to avoid numerical dispersion. The comparison is shown in Fig. 8 for different components, that is, horizontal (modulus) and vertical components. First, the mean value of our results fits well with that predicted by the attenuation relationship, at all distance ranges, for the horizontal average component and the vertical component. Second, the PSA from our simulations saturates at short distances ($< 3 \text{ km}$) from the fault plane. Third, for the horizontal average component, there are high PSAs in the fault distance range A (Fig. 8). This is the distance range that includes the basin edges, where the largest amplifications occur. The empirically predicted behaviour decreases smoothly in this range.

The most important aspect of this type of modelling is the opportunity to carry out statistical analysis of the resulting ground motion characteristics due to source related variations. In addition to the calculation of statistical moments like the variance and

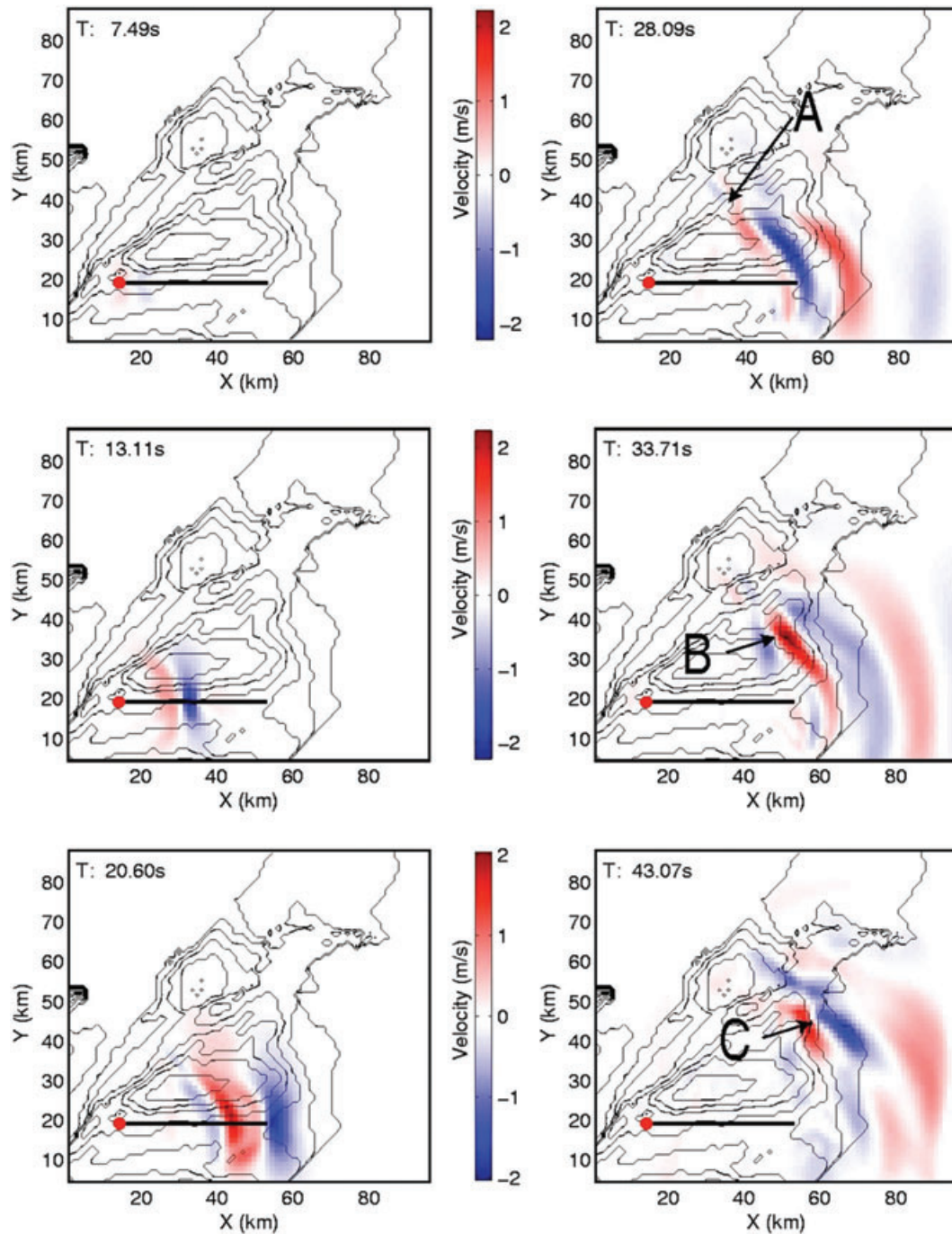


Figure 6. Velocity snapshots of y -component at different times (Hypocentre is shown as red solid circle with depth of 7.6 km from the surface). Black thin lines show the contours of isosurface of shear wave velocity at 2 km s^{-1} . Thick black line shows the fault trace. Areas A, B and C are depicted to illustrate the structure effect on wave propagation. Note the change of the colour scale.

mean motion characteristics, we can forecast deterministically, by what factor mean ground motions are exceeded in the worst case. In our opinion, this is—particularly from an engineering point of view—important information and complements the statistical relations that, in principle, allow infinite motion amplitudes (of course with very small probabilities). This is the focus of the following sections.

Two examples of the resulting PGVs in the LA basin are shown in Figs 9a and b, for the hypocentre locations H1 (5 km depth,

located at SE fault edge) and H2 (15 km depth, located towards the centre), as indicated in Fig. 3 (inset). The shallow hypocentre, with unilateral rupture propagation (H1, Fig. 9a), leads to a directivity-dominated distribution of PGVs towards the NW end of the fault, whereas the PGVs of the bilaterally propagating rupture from the deeper hypocentre (H2, Fig. 9b) shows a clear dependence on the distance from the fault, with dominant PGVs in the NW part. This is due to the main slip occurring in the northern part of the fault (see Fig. 3, inset).

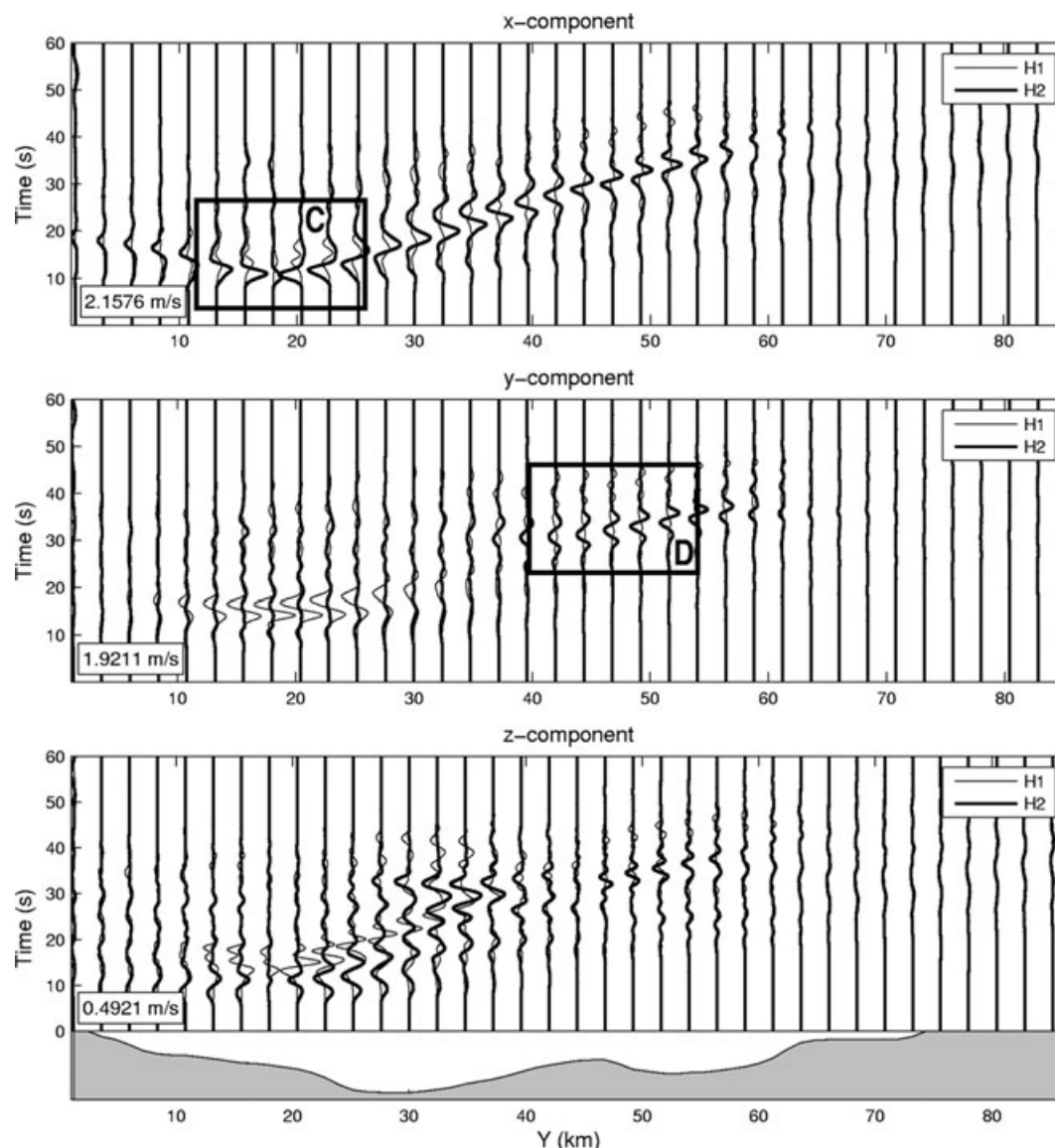


Figure 7. Velocity profile (Fig. 4 AB) simulated with two hypocenters H1 and H2 (Fig. 3, inset; the corresponding epicentres E1 and E2 are shown in Fig. 4 as black asterisks). From top to bottom are the x -, y - and z -components, respectively. The shear wave velocity isosurface depth (at 2.0 km s^{-1}) is depicted at the bottom as the shadowed area. The maximum velocity amplitude across this profile is shown with the inset number.

The parameter study in the hypocentre space allows us to extract the PGVs of all 24 simulations (Fig. 9c) containing the dominant features of the previously shown two examples, with basin wide shaking, fault-distance-dependent ground motion and peak motions above the fault area with the largest slip (asperity). The variations of the hypocentre-dependent ground motions can be expressed by the relative variance of the PGVs (absolute variance divided by the mean in per cent) at each point of the surface grid (Fig. 9d). The resulting distribution illustrates the regions in which most variations of ground motions are to be expected from the hypocentre location. These variations are symmetric around the fault edges, with some amplification from the basin edges, particularly, on the SE end. The large variations of PGV at regions off the two tips of the fault trace are also observed in Gallovič & Brokešová (2007b) for a 1-D medium, considering a frequency range much higher than ours. It is interesting to note that the largest variations of peak ground motions due to variations in hypocentre location are actually occurring not

inside the basin but either just at the edge of the basin or in the areas with bedrock.

The ratio between the maximum PGV and the mean PGV is also shown for the entire study area. For the x -component (Fig. 10, top left-hand panel) the largest ratios are observed in regions A and B near the basin edges. For the y -component (Fig. 10, top right-hand panel) large ratios are observed in regions C and D. These two regions are aligned with almost equal angle to the fault trace, possibly related to the S -wave radiation pattern. In region D, even outside the basin, high ratios are observed. For the z -component the ratios are more evenly distributed with maximum values inside the basin (region E). The largest deviation from the mean is thus predicted for the y -component of motion (factor 3) close to the edges of the basin.

We complete this study by systematically investigating the relationship between PGV and source depth for all simulated scenarios and two receivers indicated in Fig. 9 (R1, 40 km from the fault,

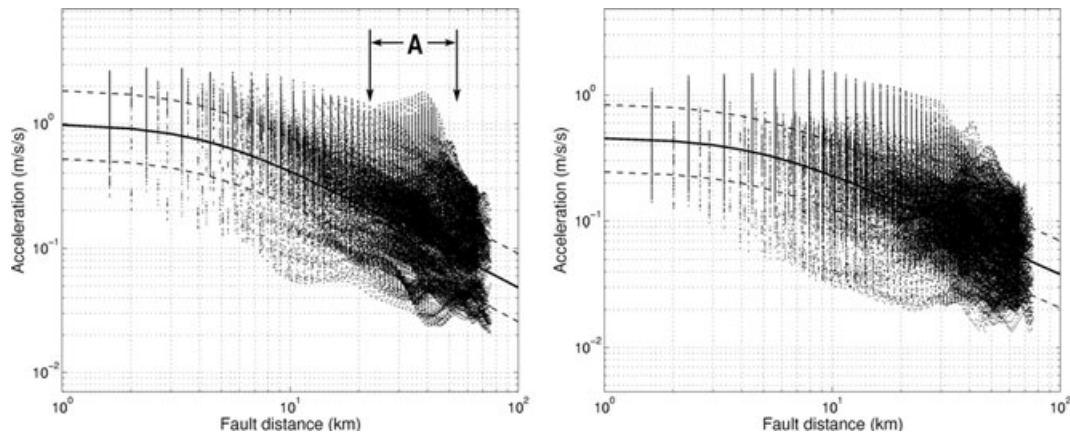


Figure 8. Comparison with the attenuation relation. Left-hand panel: Horizontal average component of acceleration response spectrum (PSA) for period of 4 s at each surface point is plotted with respect to the fault distance by small dots. Right-hand panel: Same illustration for the vertical component. The mean empirical PSA attenuation curve and its log-normal standard deviations (Campbell & Bozorgnia 2003) are shown by thick black line and thin dashed lines, respectively. Region A is further discussed in the text.

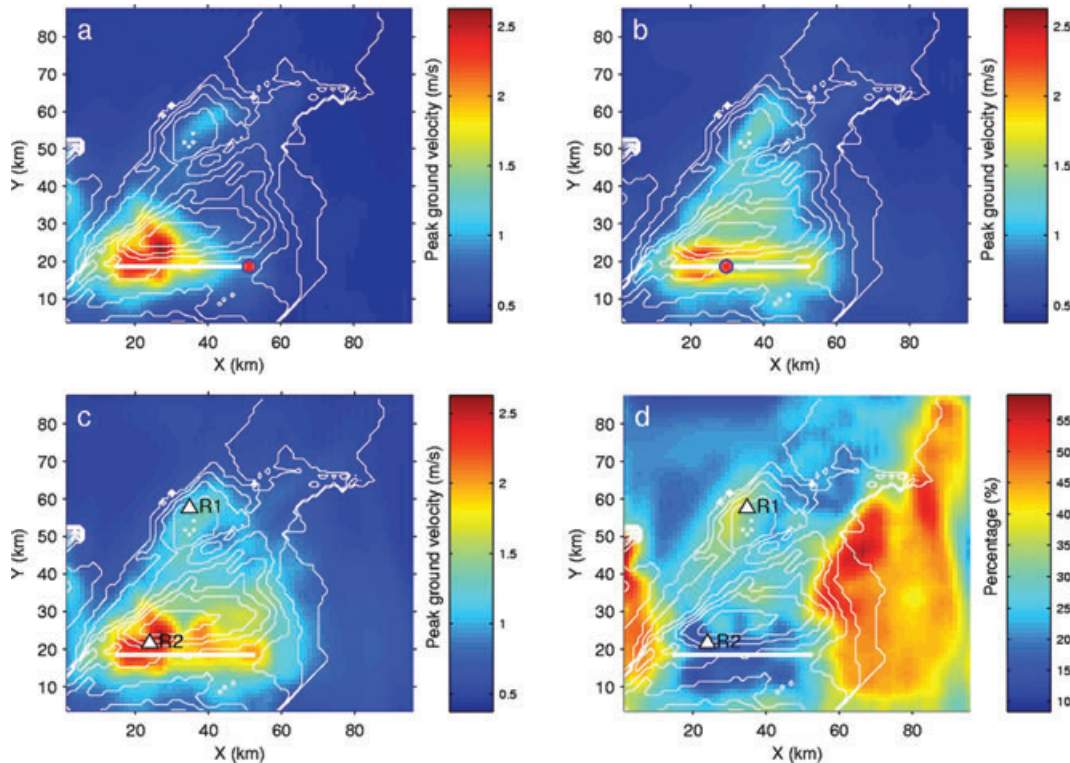


Figure 9. (a) Peak ground velocity (PGV, modulus of horizontal components) for hypocentre H1 (Fig. 3). (b) Same for H2 (Fig. 3). The epicentres are indicated as red solid circles. The straight white line indicates the fault trace. Thin white lines are contours of the seismic velocity model. (c) Maximum PGVs for all 24 simulations. (d) The ratio between the standard deviation and the mean PGV (all 24 simulations) in percent. R1 and R2 are receiver locations discussed in detail.

inside the basin; R2, above the centre of the fault). Horizontal velocity seismograms (fault-parallel component) are shown for receivers R1, R2 and four different hypocentral depths (same epicentre), as indicated in Fig. 3 (inset, white rectangle). The PGVs (and variance) for all 24 simulations at receivers R1 and R2 are displayed as a function of source depth in Figs 11c and d, respectively. For the distant receiver (R1, Fig. 11c), the mean PGV increases slightly with source depth, whereas the variance is much larger for deeper

hypocentres. Different behaviour is observed for receiver R2, close to the fault (Fig. 11d). The PGV variations are larger for the shallow hypocentres, and the mean PGV is almost independent of hypocentral depth. These results indicate the difficulties to quantify, in general, the dependence of peak ground motion characteristics from such fundamental source parameters like the hypocentre depth and motivate systematic parameter space studies for specific regions with sufficiently known structure and possible source locations.

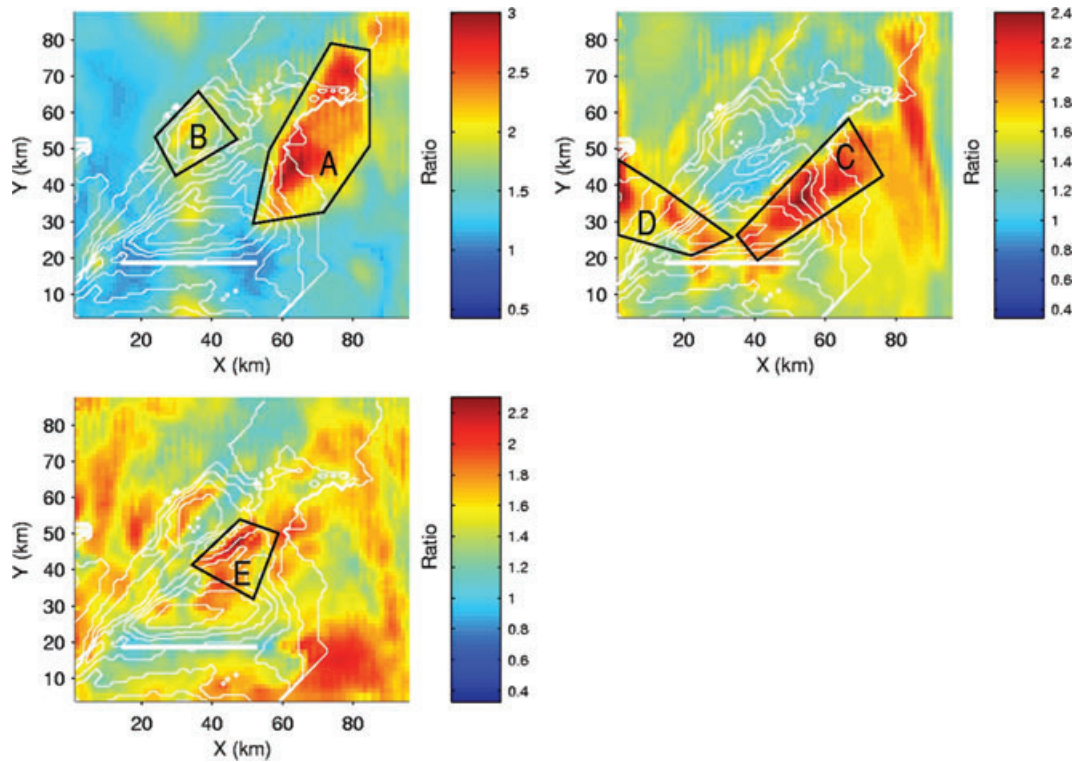


Figure 10. The ratio between the maximum and the mean PGV. Top left-hand panel: x-component. Top right-hand panel: y-component. Bottom left-hand panel: z-component. The white line indicates the fault trace. Thin white lines are contours of the seismic velocity model. Regions A, B, C, D and E are discussed in the text.

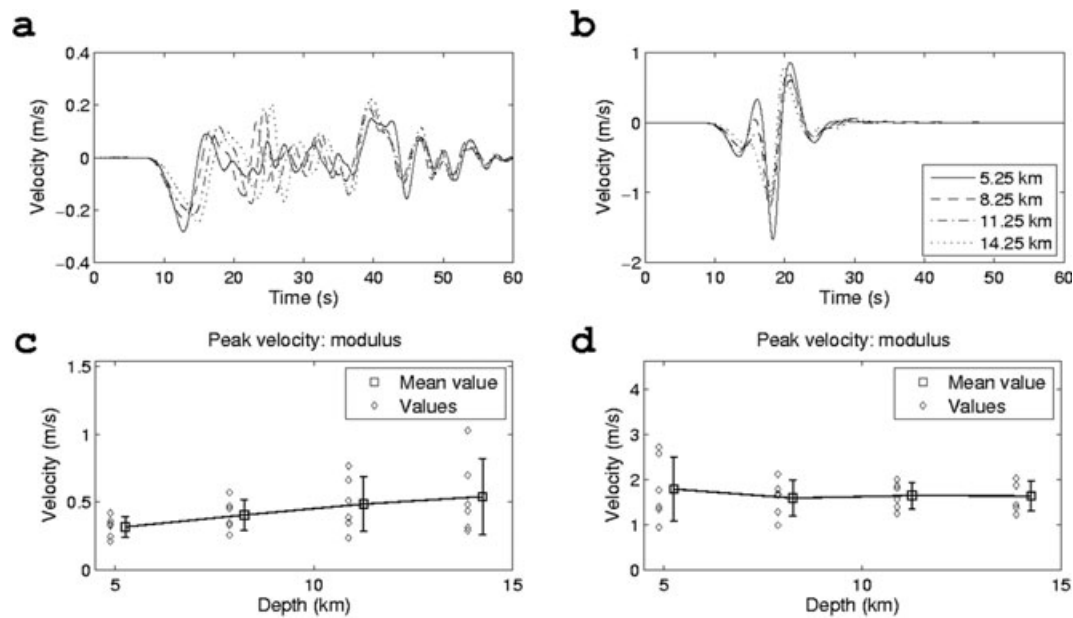


Figure 11. (a) and (b) Velocity seismograms (x-component) for the M_w 7 earthquake with same epicentre but varying source depth (see Fig. 3, inset, white rectangle) at receivers indicated in Fig. 9c. (a) R1, approx. 40 km off fault. (b) R2, close to the fault trace. (c) and (d) PGV, as well as mean and variance for all simulations. (c) R1, (d) R2. Mean value and variances are offset for illustrative reasons.

5 CONCLUSIONS

We propose the calculation of NGFs for subfaults embedded in 3-D velocity structures as an important tool to quantify local source and structure related variations of peak ground motion characteristics.

NGF databases allow, in particular, a systematic study of source related uncertainties/variations of seismic hazard relevant wavefield properties (peak ground motions, static displacements and rotations, shaking duration, etc.) due to varying slip distributions (e.g. asperity locations), slip and rupture velocities, hypocentre locations and

others. A further possibility is the combination with high-resolution slip histories from dynamic rupture simulations and the investigation of their influence on ground motions. We show for our study area that—due to finite source and basin related effects—the resulting attenuation can deviate substantially from the one predicted by empirical relations.

Our simple example on the influence of hypocentre location on the resulting ground motions indicates complex behaviour, with dependence of PGV distribution and its variation on asperity location, directionality and local structure. The high slip asperity leads to large velocity amplitudes in its neighbouring regions. Large velocities and variations are observed close to the basin edge. An important result is the observation that the largest deviations from the mean PGVs due to hypocentre location are not observed inside the basin but either near the edges or in the areas with bedrock.

This study is subject to severe limitations. Among others: (1) the fault is approximated by a vertical plane and pure strike-slip source mechanism; (2) the lowest shear-velocity (1.4 km s^{-1}) is too high to be useful for realistic hazard estimates, and the highest frequencies (0.5 Hz) are only relevant for very tall buildings and (3) we limited ourselves to investigate only one M_w 7 earthquake, happening on the same fault with the same final slip distribution.

However, the main purpose of this study is to illustrate the potential of database with NGFs to systematically investigate source related uncertainties in 3-D areas with high seismic hazard. Source related uncertainty in 3-D media is an issue that has not been addressed properly so far, partly due to limitations of computational resources. It is important to note that such NGF databases only make sense if the crustal structure is sufficiently well known, and that the NGF database would need to be recalculated with every model update. Nevertheless, the improvements of imaging technologies and thus local velocity models, combined with high-performance computing facilities, will make the proposed methodology an attractive approach for systematic local ground motion modelling studies, useful also on a larger scale, particularly, for mega-faults in subduction zones with tsunami-generating potential.

ACKNOWLEDGMENTS

This work was partially funded by the International Quality Network—Georisk (German Academic Exchange Service) and the Elite Graduate College THESIS (<http://elite.geophysik.uni-muenchen.de>). We also acknowledge support from the European Human Resources Mobility Programme (Research Training Network SPICE, <http://www.spice-rtn.org>) and the provision of computational resources through the Leibniz Computing Center Munich. ME was partly funded by the KONWIHR project and a stipend of the MunichRe. FG has been supported by Grant Agency of the Czech Republic (205/08/P013) and MSM0021620800.

REFERENCES

- Aki, K. & Richards, P.G., 2002. *Quantitative Seismology*, 2nd edn, University Science Books, New York.
- Beresnev, I.A., Atkinson, G.M., Johnson, P.A. & Field, E.H., 1998. Stochastic finite-fault modelling of ground motions from the 1994 Northridge, California, earthquake, II: widespread nonlinear response at soil sites, *Bull. seism. Soc. Am.*, **88**, 1402–1410.
- Boore, D.M., 2003. Simulation of ground motion using the stochastic method, *Pure appl. Geophys.*, **160**, 635–676.
- Bour, M. & Cara, M., 1997. Test of simple empirical Green's functions method on moderate-sized earthquakes, *Bull. seism. Soc. Am.*, **87**, 668–683.
- Campbell, K.W. & Bozorgnia, Y., 2003. Updated near-source ground-motion (attenuation) relations for the horizontal and vertical components of peak ground acceleration and acceleration response spectra, *Bull. seism. Soc. Am.*, **93**, 314–331.
- Collino, F. & Tsogka, C., 2001. Application of the PML absorbing layer model to the linear elastodynamic problem in anisotropic heterogeneous media, *Geophysics*, **66**, 294–307.
- Convertito, V., Emolo, A. & Zollo, A., 2006. Seismic-hazard assessment for a characteristic earthquake scenario: an integrated probabilistic-deterministic method, *Bull. seism. Soc. Am.*, **96**, 377–391.
- Ewald, M., Igel, H., Hinzen, K.G. & Scherbaum, F., 2006. Basin-related effects on ground motion for earthquake scenarios in the Lower Rhine embayment, *Geophys. J. Int.*, **166**, 197–212.
- Frankel, A., 1995. Simulating strong motions of large earthquakes using recordings of small earthquakes: the Loma Prieta mainshock as a test case, *Bull. seism. Soc. Am.*, **85**, 1144–1160.
- Gallovič, F. & Brokešová, J., 2004. The k^{-2} rupture model parametric study: example of the 1999 Athens earthquake, *Studia geoph. et geod.*, **48**, 589–613.
- Gallovič, F. & Brokešová, J., 2007a. Hybrid k-squared source model for strong ground motion simulations: introduction, *Phys. Earth planet. Inter.*, **160**, 34–50.
- Gallovič, F. & Brokešová, J., 2008. Probabilistic aftershock hazard assessment, II: application of strong ground motion modeling, *J. Seismology*, **12**, N. 1, 65–78, doi:10.1007/s10950-007-9070-2.
- Gerstenberger, M.C., Wiemer, S., Jones, L.M. & Reasenberg, P.A., 2005. Real-time forecasts of tomorrow's earthquakes in California, *Nature*, **435**, 328–331.
- Grant, L.B. & Shearer, P.M., 2004. Activity of the offshore Newport-Inglewood Rose Canyon fault zone, coastal Southern California, from relocated microseismicity, *Bull. seism. Soc. Am.*, **94**, 747–752.
- Graves, R.W., 1996. Simulating seismic wave propagation in 3D elastic media using staggered grid finite differences, *Bull. seism. Soc. Am.*, **86**, 1091–1106.
- Gualterri, M., Mai, P.M. & Beroza, G.C., 2004. A pseudo-dynamic approximation to dynamic rupture models for strong ground motion prediction, *Bull. seism. Soc. Am.*, **94**, 2051–2063.
- Hauksson, E. & Gross, S., 1991. Source parameters of the 1933 Long Beach earthquake, *Bull. seism. Soc. Am.*, **81**, 81–98.
- Hutchings, L. & Wu, F., 1990. Empirical Green's functions from small earthquakes—a waveform study of locally recorded aftershocks of the San Fernando earthquake, *J. geophys. Res.*, **95**, 1187–1214.
- Igel, H., Mora, P. & Rioulet, B., 1995. Anisotropic wave propagation through finite-difference grids, *Geophysics*, **60**, 1203–1216.
- Irikura, K., 1986. Prediction of strong acceleration motion using empirical Green's function, in *Proceedings of the 7th Japan Earthquake Engineering Symposium*, Tokyo, pp. 151–156.
- Jennings, C.W., 1994. *Fault Activity Map of California and Adjacent Areas with Location and Ages of Recent Volcanic Eruptions*, Map No. 6: California Geologic Data Map Series, California Division of Mines and Geology.
- Joyner, W.B. & Boore, D.M., 1986. On simulating large earthquakes by Green's-function addition of small earthquakes, *Earthquake Source Mechanism*, American Geophysical Union Monograph, **37**, 269–274.
- Kanamori, H., 1977. The energy release in great earthquakes, *J. geophys. Res.*, **82**, 2981–2987.
- Käser, M. & Gallovič, F., 2008. Effects of complicated 3D rupture geometries on earthquake ground motion and their implications: a numerical study, *Geophys. J. Int.*, **172**, 276–292.
- Kohler, M., Magistrale, H. & Clayton, R., 2003. Mantle heterogeneities and the SCEC three-dimensional seismic velocity model version 3, *Bull. seism. Soc. Am.*, **93**, 757–774.
- Levander, A.R., 1988. Fourth-order finite-difference P-SV seismograms, *Geophysics*, **53**, 1425–1436.
- Mai, P.M. & Beroza, G.C., 2002. A spatial random-field model to characterize complexity in earthquake slip, *J. geophys. Res.*, **107**(B11), 2308, doi: 10.1029/2001JB000588.

- Marcinkovich, C. & Olsen, K.B., 2003. On the implementation of perfectly matched layers in a 3D fourth-order velocity-stress finite-difference scheme, *J. geophys. Res.*, **108**, 2276–2293.
- Moczo, P., Kristek, J., Vavrycuk, V., Archuleta, R.J. & Halada, L., 2002. 3D heterogeneous staggered-grid finite-difference modeling of seismic motion with volume harmonic and arithmetic averaging of elastic moduli and densities, *Bull. seism. Soc. Am.*, **92**(8), 3042–3066.
- Olsen, K.B., 2000. Site amplification in the Los Angeles basin from 3D modelling of ground motion, *Bull. seism. Soc. Am.*, **90**, S77–S94.
- Olsen, K.B. & Archuleta, R.J., 1996. 3D-simulation of earthquakes in the Los Angeles fault system, *Bull. seism. Soc. Am.*, **86**, 575–596.
- Pitarka, A. & Irikura, K., 1996. Basin structure effects on long-period strong motions in the San Fernando Valley and the Los Angeles basin from the 1994 Northridge earthquake and an aftershock, *Bull. seism. Soc. Am.*, **86**, S126–S137.
- Spudich, P. & Archuleta, R.J., 1987. Techniques for earthquake ground-motion calculation with applications to source parametrization of finite faults, in *Seismic Strong Motion Synthetics*, pp. 205–265, ed. Bolt, B.A., Academic Press, Orlando, FL.
- Wang, H.J., 2007. Source-dependent variations of M7 earthquakes in the Los Angeles basin, *PhD thesis*. Ludwig-Maximilians-University, Munich.